China Geology 8 (2025) 265−280

China Geology

Journal homepage: http://chinageology.cgs.cn
https://www.sciencedirect.com/journal/china-geology

Timing, geometry, and kinematics of the Yilan-Yitong fault zone in the Northern Tan-Lu fault system of Northeast Asia

Liang Qiu[a,*], Yu Fu[a, b], Dan-Ping Yan[a,*], Tian-heng Wang[a], Wei Gan[a], Cheng-ming Li[a, c], Ruo-yan Kong[a, d], Rong Chu[a], Xiao-yu Chen[a], Rui Zhang[a], Shou-heng Sun[a], Xiao-yu Dong[a, e]

[a] *State Key Laboratory of Geological Processes and Mineral Resources*, *School of Earth Sciences and Resources*, *China University of Geosciences (Beijing)*, *Beijing* 100083, *China*
[b] *Sinopec Jiangsu Oilfield*, *Yangzhou* 225009, *China*
[c] *Sinoprobe Center*, *Chinese Academy of Geological Sciences*, *Beijing* 100037, *China*
[d] *Jiangxi Geological Survey and Exploration Institute*, *Nanchang* 330000, *China*
[e] *Nuclear Industry Team* 243, *Chifeng*, *Inner Mongolia* 024000, *China*

ARTICLE INFO

Article history:
Received 11 July 2023
Received in revised form 8 December 2023
Accepted 18 December 2023
Available online 19 March 2024

Keywords:
Tan-Lu fault system
Ductile shear zone
Deformation temperature
Paleopiezometry
Active fault
Major earthquake
Northeastern Asia

ABSTRACT

The largest Tan-Lu active fault system in northeastern Asia, spans approximately 3500 km in length and varies in width from 10 km to 200 km. In 1668, an earthquake with a magnitude of 8.5 occurred in Tancheng, causing the loss of over 50000 lives. To constrain the timing and process of the Tan-Lu fault system on eastern Asian margin, this study presents the field mapping, thin section observation, geochronology, and microanalysis of Weiyuanpu-Yehe ductile shear zone (WYSZ) of the northern Tan-Lu fault system. Kinematic indicators and microstructures suggest a sense of sinistral strike-slip. The deformation temperature of the mylonite is mediate to high based on the quartz deformation, c-axis fabrics. The differential stress of the shear zone is 20–40 MPa using quartz paleopiezometry. The dikes within the shear zone yielded zircon U-Pb ages of 165–163 Ma. However, due to the ambiguous geological relationship between the dikes and shear zone, additional geochronology is warranted. Since the Mesozoic era, based on the exposure of mylonite and dikes, the upper crust has been extensively eroded, exposing the ductile shear zone. Moreover, the understanding of the geometry and process of pre-existing structures has fundamental implications for predicating the potential earthquakes for the Tan-Lu fault system.

1. Introduction

The ductile shear zone is a high-strain zone that develops in the middle-lower crust under certain temperature and pressure conditions through band-shaped plastic flow (Ramsay JG and Graham RH, 1970; Ramsay J, 1980; Carreras J et al., 2010; Hu W et al., 2020). On the surface, the ductile shear zone appears as brittle faults that were gradually denuded, while the ductile manner and mylonite observed in the field are the result of later exhumation (Sibson RH, 1977; White SH et al., 1980; Cai Z et al., 2017; Qiu L et al., 2020). Large-scale ductile shear zones require continuous stress and are mostly affected by the geodynamic setting and regional tectonic events, and often occur at the boundaries of active plates or blocks (Zhu G et al., 2018). Therefore, understanding the kinematics, formation process, and mechanism of the ductile shear zone is crucial in revealing the geodynamics (Zhang B et al., 2012; Liu J et al., 2020). Various quantitatively multidisciplinary methods, such as magnetic and electron backscatter diffraction (EBSD) fabric analysis and isotopic dating, have been used based on geological observation and microscopic analysis (Simonetti M et al., 2020, 2021).

The Tan-Lu fault system extends from the Yangtze River in South China and runs through northeastern China to the Far East of Russia, covering a total length of about 3,500 km, with a width ranging from 10–200 km, and about 2400 km in length in China (Fig.1a; Deng YF et al., 2013; Clinkscales C et al., 2019; Yan DP et al., 2020). This fault system represents

First author: *E-mail address*: qiul@cugb.edu.cn (Liang Qiu).
* Corresponding author: *E-mail address*: qiul@cugb.edu.cn (Liang Qiu); yandp@cugb.edu.cn (Dan-Ping Yan).

Literary editor: Xi-jie Chen
doi:10.31035/cg20230060
2096-5192/© 2025 China Geology Editorial Office.

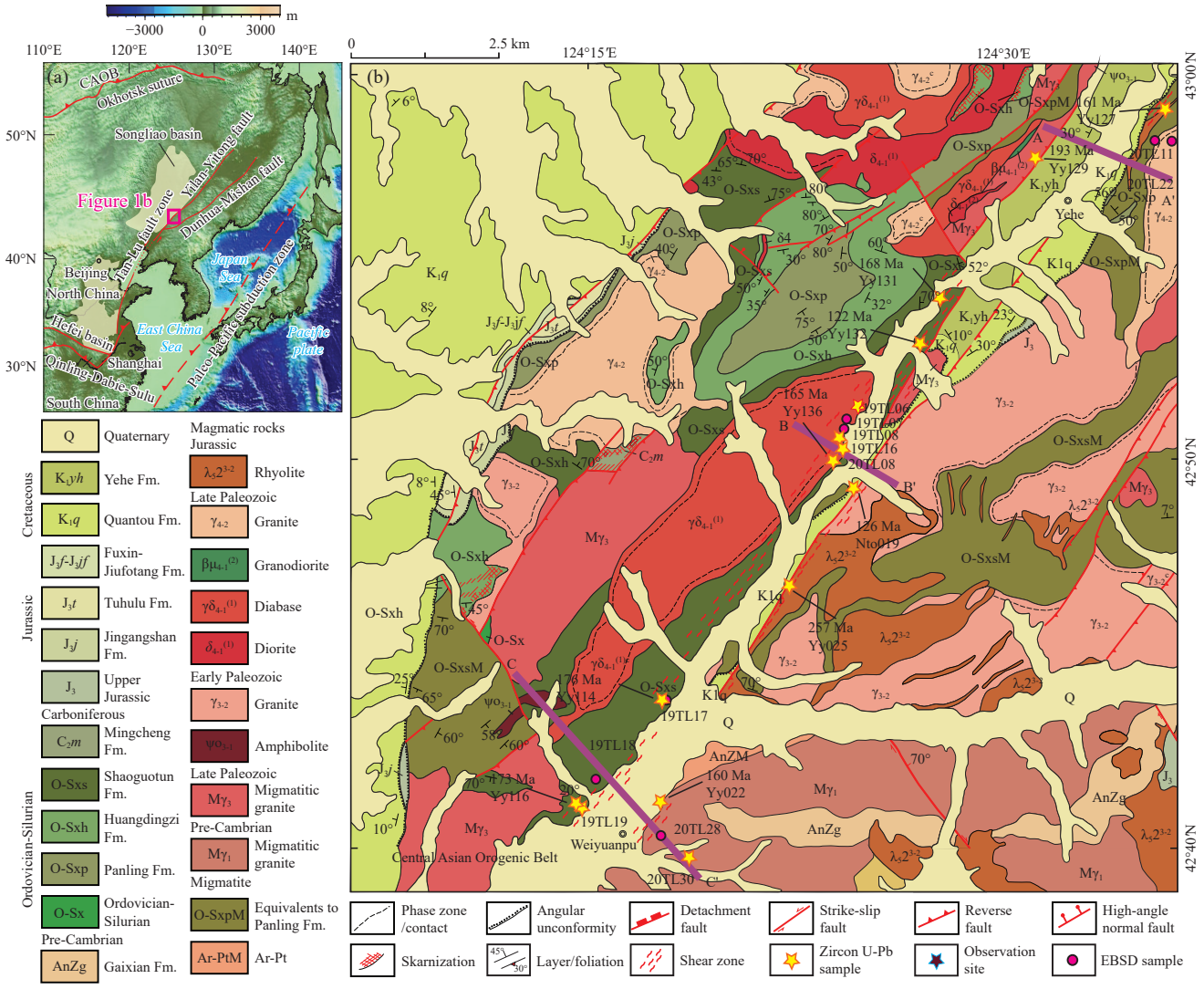

Fig. 1. Tectonic sketch and geological map of the Yilan-Yitong fault zone in northern segment of the Tan-Lu fault system. (a) Tectonic sketch showing major continents and the location of study area; (b) Geological map of the Yilan-Yitong fault zone of Tan-Lu fault system (compiled after BGMRLN, 1973, 2014). Abbreviation: CAOB, Central Asian Orogenic Belt.

a significant and seismically active belt, which has been attributed to the occurrence of noteworthy earthquakes, such as the 1668 M 8.5 Tancheng earthquake, the 70 BC M_S 7.0 Zhucheng earthquake, and the 1969 M 7.4 Bohai earthquake (Zhu G et al., 2015). The fault system comprises NE-trending strike-slip secondary faults through the lithosphere in northeastern Asia (Xu JW et al., 1987, 1994; Fig. 1a) and plays a significant role in East Asian tectonics. The middle and southern segments have been interpreted to have developed during the Middle Triassic Qinling-Dabie-Sulu orogeny due to the collision of North China and South China blocks (Hacker B et al., 2000; Faure M et al., 2003; Zhao T et al., 2016). Previously proposed models include a syn-exhumation transform fault (Okay and Şengör, 1992), an indenter boundary (Yin A and Nie S, 1993), a tear fault triggered by upper-crustal overthrust (Li Z, 1994; Lin, 1995; Chang E, 1996), or a rotated suture zone (Gilder SA et al., 1999). The complex evolutionary process of the northern Tan-Lu fault system in the continental margin is closely related to the subduction of the Paleo-Pacific plate in the Middle Jurassic to Early Cretaceous (Zhu G et al., 2018; Li Y et al., 2019). Furthermore, Liu C et al. (2018) proposed that the Dunhua-Mishan fault, as the east branch of the northern Tan-Lu fault system, was formed with sinistral strike-slip in the Early Cretaceous. For the Yilan-Yitong fault zone as the western branch, Gu CC et al. (2016, 2017) proposed deformation stages including Early Cretaceous sinistral strike-slip, Early Cretaceous-Paleogene extension, Paleogene compression, Neogene subsidence, and Quaternary compression.

This contribution of this paper focuses on the architecture and development of the Weiyuanpu-Yehe segment of the Yilan-Yitong fault zone as the northern Tan-Lu fault system. Combining structural data, the results of this study will shed light on understanding the origin mechanism and evolution history of the northern Tan-Lu fault system and provide evidence for the Mesozoic tectonic evolution of eastern Asia.

2. Geological setting

2.1. Regional geology

During the orogeny until the Late Triassic, the Central

Asian Orogenic Belt collided with the Siberian craton to the north side and the North China block to the south side (Xiao WJ et al., 2003; Yan DP and Qiu L, 2020). Subsequently, during the Permian-Triassic Qinling-Dabie-Sulu orogeny, the South China block collided with the North China block (Fig. 1a). The NE- and NNE-trending fold-thrust belt and magmatic arc on the continental margin overprinted the previous structures during the Jurassic to Early Cretaceous due to the subduction of the Paleo-Pacific plate (Li S et al., 2012, 2019; Qiu L et al., 2018, 2022; Suo Y et al., 2020). This resulted in Cretaceous extension on the surface due to oblique subduction and subsequent steepening and flattening of slabs (Zhu G et al., 2018; Kong RY et al., 2020; Liang S et al., 2020; Yan D et al., 2021).

The basement of North China block is comprised of Archean TTGs, Proterozoic granulite, metaclastic rock, and marbles, while the cover sequences are carbonate and clastic rocks (Qiu L et al., 2018). Extensive Late Jurassic-Early Cretaceous magmatic rocks are widely distributed in northeastern China, and in the Cretaceous and Paleogene, the rollback of the Paleo-Pacific plate led to back-arc extension and the formation of rift basins, such as the Songliao basin (Ren J et al., 2002; Meng E et al., 2010). Additionally, the Yilan-Yitong fault zone underwent extension, resulting in a series of grabens such as Yehe, Weiyuanpu, and Shulan grabens (Fig. 2).

The study area in the eastern Central Asian Orogenic Belt exposes Precambrian basement and Lower Paleozoic to Mesozoic cover sequences. The Precambrian basement is dominated by migmatite, schist, and granulite, and the Lower Paleozoic consists of schist, marble, and limestone. The Jurassic strata comprise shale, seam, sandstone, basalt, tuff, and rhyolite, and the Cretaceous strata consist of terrigenous mudstone, sandstone, and conglomerate. In the study area, Paleozoic biotite granite and monzogranite, and Triassic and Jurassic monzogranite, granodiorite, and diorite are exposed (Fig. 1b; Wu FY et al., 2011; Zhang S et al., 2020).

2.2. Geology of Tan-Lu fault system

The Tan-Lu fault system straddles multiple geological blocks, including the South China block, North China block, the Songliao block, Qinling-Dabie-Sulu, the Yanshan, and Central Asian Orogenic belts (Qiu L et al., 2022; Li C et al., 2023). The Tan-Lu fault system has undergone multiple stages of evolution, including strike-slip activities, extensions, and thrust faulting. Strike-slip ductile shear zones have been developed and exposed in the basement and both sides of the Yehe graben (Zhu G et al., 2005, 2015). The fault system was active during the Cretaceous-Early Cenozoic and controlled the formation of several basins, such as the Songliao and Hefei basins. The formation and structural evolution of the Tan-Lu fault system have had a significant impact on the tectonic evolution of northeastern Asia and are a response to the geodynamics of the subduction of the Paleo-Pacific plate (Zhu G et al., 2018).

3. Structures of Weiyuanpu-Yehe shear zone

The ductile shear zone is primarily exposed within Permian and Jurassic granite plutons and early Paleozoic strata (Fig. 1b). This zone developed within the migmatite and formed the granitic protomylonite. The mineral assemblage consists of fine-grained K-feldspar (40%), quartz (30%), hornblende (15%), biotite (10%), and other minerals (5%). The diameter of K-feldspar porphyroclasts is generally greater than 2 mm. The intrusion of undeformed veins and the shear zone boundary between the mylonitic belt and the undeformed granite are clearly visible (Fig. 2). To the east of Yehe town, there is a 2.5 km long strike-slip ductile shear zone exposed in the Mesozoic granite plutons. The mineral compositions of granitic protomylonite and granitic mylonite are similar to the western side of the ductile shear zone near Weiyuanpu town. Additionally, undeformed diorite porphyrite dikes intruded into the mylonite zone (Fig. 2).

3.1. Macro-scale structures

To decipher the WYSZ, three transects - A-A', B-B', and C-C' - were observed (Fig. 2). The transect A-A', located near Yehe town, crosses the Lower Paleozoic granitic migmatite, Cretaceous Yehe Formation, Quaternary and Paleozoic granites from west to east. On the west side of the profile, there is a flesh-red granite set containing K-feldspar (40%) + quartz (45%) + biotite/hornblende (15%). The cross-cutting relationship is complex, including the development of at least two sets of cleavage and multiple-stage intrusion of diabase and quartz vein. The normal fault has a hanging wall of the Cretaceous Yehe Formation that consists of feldspar sandstone and a granitic footwall that developed NE-verging secondary faults and folds. The fault plane dips to 300° with a dip angle of 25°. A 100 m-wide granitic mylonitic belt occurred in the Paleozoic granite at the eastern edge of the Yehe graben (Fig. 2a). The S-C fabrics observed at the outcrop are defined by feldspar porphyroclasts. K-feldspar appears as “δ” and “σ” types of porphyry clasts, indicating a sense of sinistral shearing (Fig. 2b). The mylonitic foliation dips to 320° with a dip angle of 65° (Fig. 2c), which is consistent with the foliation of the west side of the ductile shear zone. Most of the mineral lineation plunges to 65° NE at an angle of 20°. The level of mylonization decreases from the center of the graben to the outside.

The 4.5 km-long and NW-SW-trending transect B-B' is located in the middle of the WYSZ and cuts through the Mesozoic granite, Paleozoic monzonitic granites, and Quaternary (Fig. 2d-e-f). The Mesozoic granite is widely exposed on the west side of the graben and has a mineral assemblage of K-feldspar (40%), quartz (35%), biotite (15%), amphibole (5%), and other minerals (5%). A 200 m-wide mylonite belt shows granitic protomylonite to granitic mylonite from west to east (Fig. 2d). The intense deformation and mineral elongation gradually increase from NW to the graben, indicating that the center of the shear zone covered by the Cretaceous is located in the middle of the graben. The

Fig. 2. Transects, field photographs, and projections of structural elements through the Weiyuanpu-Yehe shear zone. (a) Fault zone dominated by shear bends, breccia, and gouge (stop 20TL22); (b) Granitic protomylonite (stop 20TL22); (c) Outcrops of granitic mylonite of the ductile shear zone on the west side (stop 19TL07); (d) S-C fabrics that were defined by feldspar and elongated quartz and hornblende and biotite, indicating a sinistral strike-slip (19TL08); (e) Undeformed porphyrite dike intruded into the granitic mylonite in the western side of shear zone (stop 19TL08); (f) Undeformed diorite porphyrite dikes (stop 19TL08); (g) S-C fabrics in protomylonite (stop 19TL18); (h) Potassium feldspar asymmetry porphyroclasts in protomylonite (stop 20TL28); (i) dike intruded into the granite within the shear zone near the Weiyuanpu town (stop 20TL30); (j) Granitic mylonite defined by mineral lineation (stop 19TL19).

mylonitic foliation of the ductile shear zone in this area dips to NW uniformly with a dip angle of 320°, and the lineation plunges to NE. The Quaternary stratum as a part of the hanging wall was separated from the granite of the footwall by a normal fault. The fault plane dips to 225° with a dip angle of 70°.

The southernmost end of the WYSZ is traversed by transect C-C', which cuts through the early Paleozoic granitic migmatite, Paleozoic Shaoguotun Formation, and Quaternary deposits (Fig. 2). Field observations indicate that the Early Paleozoic migmatite on the western side of the Weiyuanpu graben is angular unconformably overlain by the quartz schist of the Paleozoic Shaoguotun Formation and is undeformed. The granite pluton, situated to the east of the Shaoguotun Formation, exhibits a medium- to coarse-grained texture that gradually transitions to mylonite close to the Weiyuanpu graben (Figs. 2i-j). This is evidenced by the reduction in mineral particle size and the oriented arrangement of biotite and hornblende. The mylonitic belt, characterized by quartz aggregates in the form of bands, mylonitic foliation, and mineral lineation, is 100 m wide and is covered by thick Quaternary alluvium in the Weiyuanpu graben. The mylonitic foliation primarily dips to 324° with a dip angle of 30° (Fig. 2g-h). The Cretaceous Quantou Formation sandstone exposed on the northern Weiyuanpu graben and is situated below the Quaternary deposits. On the east side of the profile, the Mesozoic granitic migmatite displays a 150 m-wide mylonite belt close to the ascending plate of the Weiyuanpu graben. The foliation dips to 145° with a dip angle of 30°, and the mineral lineation plunges to the south at an angle of 15°–30° (Fig. 2i; transect C-C').

The shear zone exhibits protomylonite, mylonite, and ultramylonite from the margin to the center. The mylonite foliation on the east side of the WYSZ dips to 300°–340° with dip angles ranging from 35° to 85° and an average dip angle greater than 60°. Most of the lineation plunges to the northeast, while a minority plunges to the southwest. K-feldspar fragments and biotite in the mylonitization zone constitute S-C fabrics, indicating sinistral shearing. Field outcrops of the sheared granite pluton display two groups of cleavages that dip to 326° and 221° with dip angles of 81° and 53° (Fig. 2), respectively. The foliation of the WYSZ exposed on the east side of Weiyuanpu town dips to the southwest at an angle of about 30°. The mineral lineation is well-developed and uniformly plunges to the south at an angle of 15°–30°. Mylonitization decreases from the center of the graben towards the outside.

3.2. Micro-structures

Plastic deformation leads to various microstructures in the WYSZ, observed in field outcrops and under thin-sections (Fig. 3). S-C fabrics, feldspar porphyroclasts, tails, bookshelf structures, and mica fish structures indicate the sense of shearing, observed in field outcrops and under the microscope. During shearing, elongated quartz, centimeters-long K-feldspars, biotite, and translucent hornblende align and arrange themselves to define the mineral lineation. Quartz grains form quartz bands, with aligned quartz grains

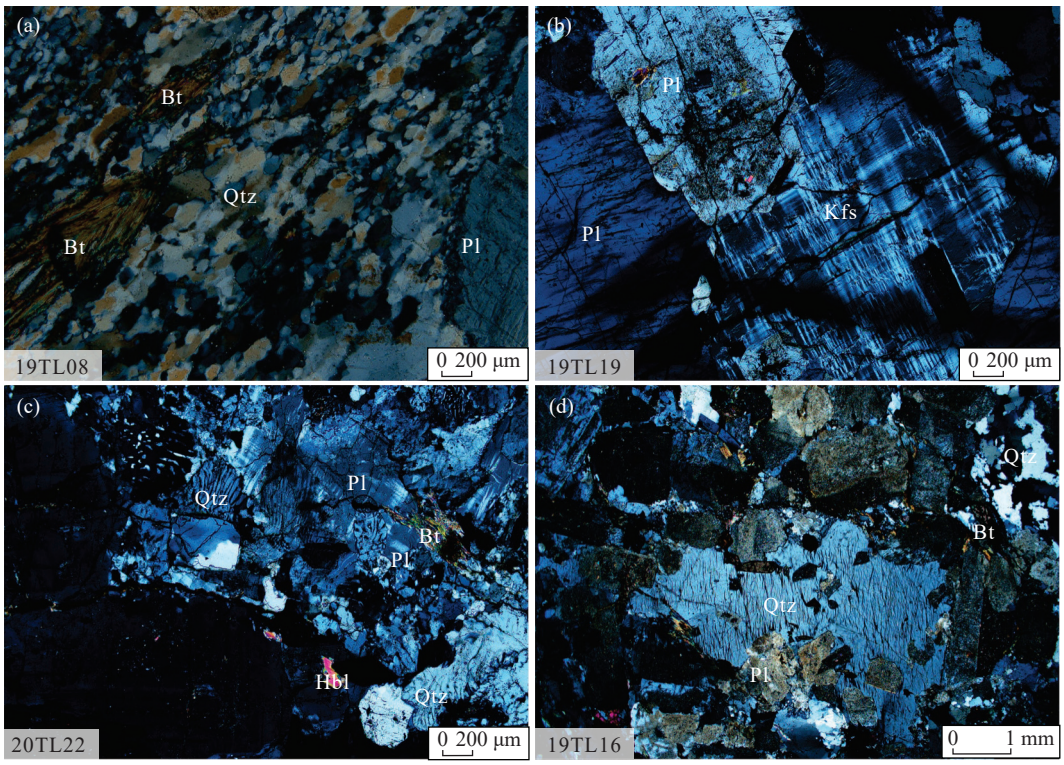

Fig. 3. Photomicrographs showing mineral assemblage and microstructures for mylonites. (a) Dynamic recrystallization of quartz; (b) Lattice twin of microplagioclase; (c) Feldspar vermicular structure; (d) Quartz "S"-shaped deformation pattern. Mineral abbreviation: Kfs, K-feldspar; Qtz, quartz; Pl, plagioclase; Bt, biotite; Hbl, hornblende.

displaying a clear crystal surface and sweeping undulose extinction. Plagioclase shows lattice twins, and feldspar displays a vermicular structure with a sericited and fragmented surface.

3.2.1. Deformation of quartz

The deformation of quartz in the WYSZ leads to quartz ribbons, gridiron twinning, deformation lamella, and vermicular texture. Dynamic recrystallization of quartz is common and primarily accommodated by subgrain rotation and grain boundary migration. The neoblasts recrystallized quartz grains are equally distributed in size, with straight boundaries and a typical core-mantle structure. The core consists of low-strain quartz remnants that produce wavy extinction, and the mantle consists of new particles or aggregates of dynamically recrystallized quartz. The quartz in the mylonite and protomylonite displays different crystal morphology, and the quartz bands are mainly composed of quartz crystals or aggregates, with quartz ribbons in the center showing stretching, elongation, and preferred orientation. Two groups of nearly perpendicular poly-sheet twin crystals combine to form lattice twin crystals, while gridiron twinning of plagioclase also occurs. Vermicular quartz forms due to the deformation of feldspar during mylonization.

3.2.2. Shear sense indicators

Microstructures including rotating fragmentation systems, S-C fabrics, mica fish, and bookshelf structures suggest consistent sinistral shear observed from field outcrops (Fig. 4). Elongated deformed feldspars and quartz particles form the S foliation, and dark minerals such as biotite align to form the C foliation, indicating a sinistral shearing. Porphyry clasts are widely developed in the ductile shear zone, mainly composed of feldspar plaques and tailings, with "σ" and "δ" type rotated porphyroclasts, indicating sinistral shearing. Brittle fracturing of feldspar leads to bookshelf structures with the inclination direction suggesting a sense of shearing. The upper and lower pieces of mica slide and rotate during shearing, forming an asymmetric mica fish that indicates left-lateral sense of shear.

4. Analytical methods

4.1. The Electron backscattered diffraction (EBSD)

The EBSD analysis of the samples was performed using a FEI Quanta 450 FEG Field Emission Scanning Electron Microscope and an Oxford Nordlys F+EBSD high-speed detector in the Continental Tectonics and Dynamics Microzone Laboratory at the Institute of Geology, Chinese Academy of Geological Sciences. The data was acquired in a surface scan mode and processed using HKL Channel 5 and the open-source MATLAB toolbox MTEX, as reported by Bachmann F et al. (2010a, 2010b, 2011). Grain boundaries were defined by misorientation angles >10°. Dauphiné twin boundaries were detected by 60° rotations around c-axis. Pole figures of quartz c-axis are plotted in lower hemisphere, equal area and constructed using one point per grain. Root mean square grain sizes were calculated and used to generate differential stress with Cross AJ et al. (2017) piezometer. The error of grain sizes and differential stress were reported as a single standard deviation.

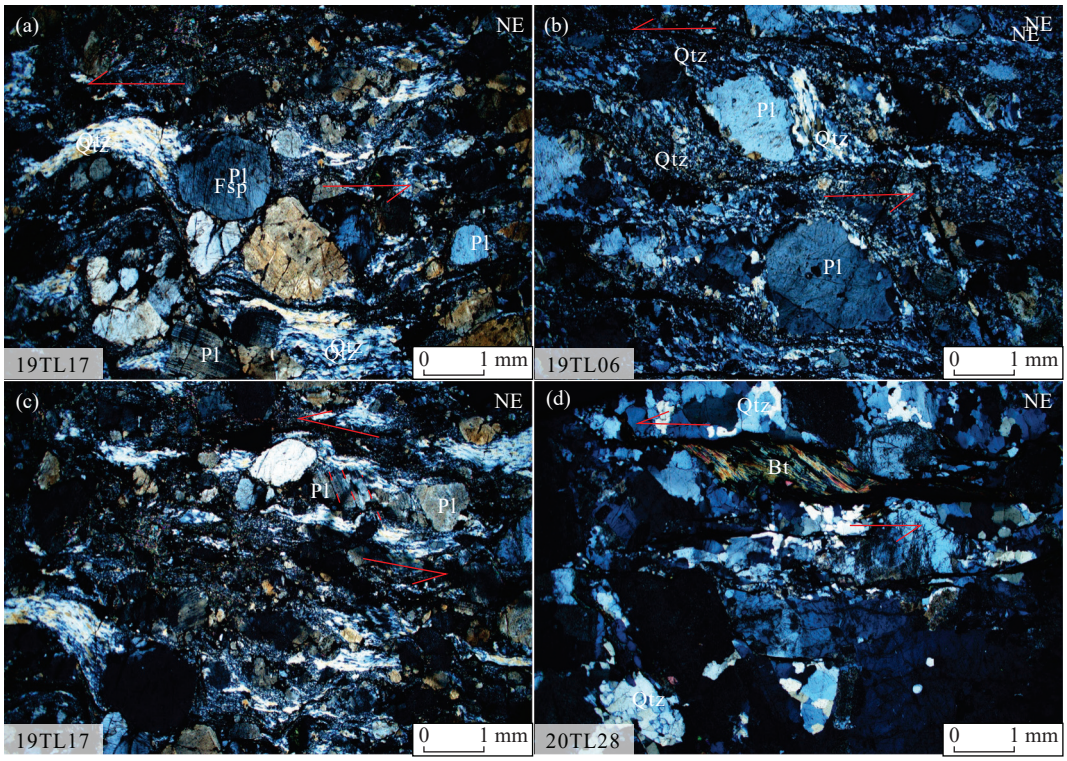

Fig. 4. Photomicrographs showing shearing indicators in mylonites. (a)–"δ" type asymmetry porphyroclasts; (b)–"σ" type asymmetry porphyroclasts; (c)–Domino structure; (d)–Mica fish.

4.2. Zircon U-Pb analyse

Zircon U-Pb dating was performed using LA-ICPMS at Beijing GeoAnalysis CO., LTD. The Resolution SE model laser ablation system (Applied Spectra, USA) was equipped with an ATL (ATLEX 300) excimer laser and a Two Volume S155 ablation cell. This laser ablation system was coupled to an Agilent 7900 ICPMS (Agilent, USA). For detailed tuning parameters, please refer to Thompson J et al. (2018). Zircons were mounted in epoxy discs, polished to expose the grains, ultrasonically cleaned in ultrapure water, and subsequently cleaned again before analysis using AR grade methanol. Pre-ablation was carried out for each spot analysis using 5 laser shots (0.3 μm in depth) to eliminate potential surface contamination. The analysis was conducted using a 30 μm diameter spot at 5 Hz and a fluence of 2J/cm^2. Data reduction was performed using the Iolite software package (Paton C et al., 2010). Zircon 91500 served as the primary reference material, and GJ-1 as the secondary reference material. Zircon 91500 was analyzed twice, and GJ-1 was analyzed once every 10–12 analyses of the sample. Typically, 35–40 seconds of the sample signals were acquired following a 20-second gas background measurement. The exponential function was applied to calibrate downhole fractionation (Paton C et al., 2010). NIST 610 and 91Zr served as external reference material and internal standard element, respectively, for calibrating trace element concentrations. The measured ages of the reference materials in the batch are as follows: 91500 (1061.5 ± 3.2 Ma, 2σ), GJ-1 (604±6 Ma, 2σ), aligning well with the reference values within the defined uncertainty. Zircon Plesovice, dated as an unknown sample, yielded a weighted mean $^{206}Pb/^{238}U$ age of (337.5 ± 1.5 Ma, 2σ), in good agreement with the reference value within the specified uncertainty (Sláma J et al., 2008).

5. Analytical results

5.1. Quartz microstructures and deformation temperatures

The microstructures of quartz present in the WYSZ provide a useful estimate of the deformation temperature. Specifically, the quartzes in the granitic protomylonite and granitic mesomylonite located on the west side of the WYSZ exhibit ribbon-like, elongated recrystallized structures that are distributed along the shear bend. These features indicate a medium to high deformation temperature of mylonite (Stipp M et al., 2002; Table 1). On the east side of the WYSZ, the granitic mylonite near Yehe town shows elongated quartz neoblasts that are consistent in size with straight and smooth grain boundaries. The overall core-mantle structure of this mylonite is formed by the subgrain rotating recrystallization process (Fig. 5), suggesting the coexistence of two recrystallization types and medium deformation temperature (Stipp M et al., 2002). Therefore, the recrystallization of quartzes in mylonite serves as a first-order constraint on the medium to high temperature of mylonitization during the formation of the WYSZ.

5.1.1. Pole figures of quartz c-axis fabrics

Samples of granitic protomylonite and mesomylonite were collected from the west and east sides of the WYSZ, respectively. Seven thin sections were selected for EBSD analysis, including samples 19TL07, 19TL08-2, 19TL17-1, and 19TL18-1 from the west side, and samples 20TL11-1, 20TL22-1, and 20TL28-1 from the east side of the WYSZ. Quartz CPO pole figures from the seven quartz-rich samples, with greater than 40% indexed quartz modes and/or quartz bands/aggregates, show sinistral shear sense (19TL07, 19TL17-1, 20TL11-1, and 20TL22-1) and dextral shear sense (19TL08-2, 19TL18-1, and 20TL28-1) (Fig. 6). CPOs of quartzes from 19TL07, 19TL08, 19TL17, and 19TL18 display point maxima patterns close to X-direction for c-axis and asymmetry girdle for a-axis, which indicate prism <c> dominant slip system. The c-axis fabrics of samples 20TL11 and 20TL22 have asymmetry girdles and weak point maxima close to Y. Poles to a-axis of sample 20TL11 have a great circle with a maximum close to X, and sample 20TL22 has a single maximum at the middle of X and Z at the XZ plane. These two samples suggest a mixed slip system of prism<a> and rhomb<a>.

5.1.2. Quartz paleopiezometry

In this section, the EBSD experimental data of sample 19TL07 were analyzed using the RexRelict_v2 program in the MTEX toolbox of Matlab software. The mineral phase diagram revealed that quartz was the main substance in the area, followed by feldspar. Poorly indexed white areas were excluded from the analysis. Fig. 7a-b shows the misorientation distribution (GOS) of each grain, with the black line representing the residual grain boundary. Recrystallized grains with less internal distortion cross the GOS threshold and appear blue. A balanced curve was used to calculate the GOS threshold, which is identified by the inflection points separating the recrystallized grains from the residual grains. This process eliminated the influence of Dauphiné twin crystals, resulting in a graph where the red area represents residual grains and the blue area represents recrystallized grains (Fig. 7c).

The grain size distribution histogram of sample 19TL07 is shown in Fig. 7. Both the grain size histogram and the misorientation graph indicate that the recrystallized grains are relatively small, while the residual grains are mostly large. The fine residual grains may represent recrystallized grains formed in the early stage of deformation and accumulated strain during the deformation process. The separation of recrystallized grains based on GOS is reasonable (Cross AJ et al., 2017). The RMS recrystallized quartz grain sizes for samples 19TL07, 19TL08, 19TL17, 19TL18, 20TL11, 20TL22, and 20TL28 range from 44.8–124 μm, with stresses of 19.4–39.9 MPa calculated using D=103.91 ± 0.41*σ−1.41 ± 0.21 (Cross AJ et al., 2017). The dRMS for sample 19TL07 was calculated to be 63.6 ± 28.9 μm, resulting in a differential stress of 31.2 MPa. Similarly, sample 19TL08 has dRMS = 53.5 ± 26.5 μm and a differential stress of 35.3 Mpa; sample 19TL17 has dRMS = 44.8 ± 16 μm and a differential stress of

Table 1. A compilation of dike samples and microscopic observation from mylonites in the Yilan-Yitong shear zone.

Sample ID	Rock type	Mineral assemblage	Microstructure-quartz	Estimated T°C	Source
19TL07-1	Granitic mylonite	Quartz (35%) + K-feldspar (40%) + Muscovite (15%) + Biotite (5%) + amphibole (5%)	SGR	High-T	This study
19TL08-2	Granitic mylonite	Plagioclase (40%) + Quartz (35%) + Biotite (10%) + Muscovite (15%)	GBM/SGR	High-T	This study
19TL16	Granitic mylonite	Plagioclase (40%) + Quartz (35%) + Biotite (15%)	BLG/SGR	Median-T	This study
19TL17-1	Granitic mylonite	Plagioclase (50%) + Quartz (35%) + Biotite (5%) + Muscovite (5%)	GBM	High-T	This study
19TL18-1	Granitic protomylonite	Quartz (50%) + K-feldspar (35%) + Biotite (10%) + Muscovite (10%)	GBM	High-T	This study
19TL19-1	Granitic protomylonite	Quartz (50%) + Plagioclase (15%) + K-feldspar (15%) + Mica (5%)	GBM	High-T	This study
20TL11-1	Granitic mylonite	K-feldspar (40%) + Quartz (35%) + Biotite (10%) + amphibole (10%)	GBM	High-T	This study
20TL22-1	Granitic mylonite	Plagioclase (50%) + Quartz (35%) + Biotite (5%) + amphibole (5%)	GBM	High-T	This study
20TL28-1	Granitic mylonite	Quartz (35%) + Plagioclase (20%) + Biotite (15%)	GBM	High-T	This study
20TL08	Undeformed dyke	Calcite (80%) + Plagioclase (5%) + Biotite (5%)	none	none	This study
20TL30-1	Undeformed dike	Plagioclase (65%) + Biotite (10%) + Matrix (20%)	none	none	This study
20TL30-2	Undeformed dike	Plagioclase (85%) + Biotite (10%)	none	none	This study
YY022	Protomylonite	P(65%):Fel+Qz+Bi+Ep M(35%):Qz+Bi+Ch	SR	400–450	Gu CC et al., 2016
YY105	Protomylonite	P(80%):Fel+Qz+Bi+Ep M(20%):Qz+Bi+Ch	BLG+SR	400	Gu CC et al., 2016
YY025	Mylonite	P(45%):Fel+Qz+Bi M(55%):Qz+Bi+Ch	SR	400–450	Gu CC et al., 2016
YY112	Mylonite	P(40%):Fel+Qz+Bi M(60%):Qz+Fel+Bi+Ch	SR	400–450	Gu CC et al., 2016
YY113	Mylonite	P(30%):Fel+Qz+Bi M(70%):Qz+Fel+Bi+Ch	SR	400–450	Gu CC et al., 2016
YY114	Mylonite	P(25%):Fel+Qz+Bi M(75%):Qz+Fel+Bi+Ch	SR	400–450	Gu CC et al., 2016
YY115	Mylonite	P(30%):Fel+Qz+Bi M(70%):Qz+Fel+Bi+Ch	SR+GBM	450–500	Gu CC et al., 2016
YY116	Mylonite	P(20%):Fel+Qz+Bi M(80%):Qz+Fel+Bi+Ch	SR	400–450	Gu CC et al., 2016
YY136	Mylonite	P(45%):Fel+Bi M(55%):Qz+Bi	SR	400–450	Gu CC et al., 2016
YY049	Protomylonite	P(65%):Fel+Oz+Bi M (35%):Qz+Bi	BLG	350–400	Gu CC et al., 2016
YY051	Protomylonite	P(80%):Bi+Qz+Fel+Ms M(20%):Qz+Bi+Ms	BLG	350–400	Gu CC et al., 2016

39.9 Mpa; sample 19TL18 has dRMS = 75.4 ± 42.6 μm and a differential stress of 27.6 Mpa; sample 20TL11 has dRMS = 116 ± 52.8 μm and a differential stress of 20.4 Mpa; sample TL2022 has dRMS = 111 ± 68 μm and a differential stress of 21.1 Mpa, and sample 20TL28 has dRMS = 124 ± 65.9 μm and a differential stress of 19.4 Mpa (Table 2).

5.2. Zircon U-Pb age of dikes

A total of three samples, 20TL08, 20TL30-1, and 20TL30-2, were collected from diorite porphyrite dikes within or near the WYSZ. Twenty zircon grains were analyzed on sample 20TL08 with a total of 20 spots. According to the CL image, the zircon grains are mostly grey, and a few are off-white and dark black with various shapes, most of which are uherdral and prismatic (Fig. 8a). The zircon grains have a length of 150–200 μm with length to width ratio ranging from 2∶1 to 3∶1. Th/U ratio in sample 20TL08 is generally greater than 0.4. The calculated $^{206}Pb/^{238}U$ weighted mean age is163.9±2.6Ma(n=19;MSWD=3.4)(Figs.9a–b;Supplementary Table S1).

The zircon grains of sample 20TL30-1 are mainly euhedral, pyramidal, and prismatic shapes, and the aspect ratio is mostly between 1∶1-1∶3 in the CL images (Fig. 8b). The gray and black zircons are about 70–120 μm, and shows oscillatory zonal textures. The Th/U ratio is greater than 0.5. The 10 analytical points yielded a $^{206}Pb/^{238}U$ weighted mean age of 165.4 ± 4.0 Ma (n=9; MSWD=3.6) (Figs. 9c–d; Supplementary Table S1).

The zircon grains from sample 20TL30-2 are euhedral with pyramidal and prismatic shapes with aspect ratios of 1∶1–1∶3 (Fig. 8c). The Th/U ratio ranges from 0.18 to 1.24. The 11 spots show a concordant age of 163.1 ± 0.9 Ma (MSWD=0.2) and a weighted mean age of 163.1 ± 0.9 Ma (*n*=11; MSWD=0.93) (Figs. 9e–f; Supplementary Table S1).

6. Discussion

6.1. Deformation of the WYSZ

The deformation of the WYSZ can be characterized by various kinematic indicators, including the S-C fabrics

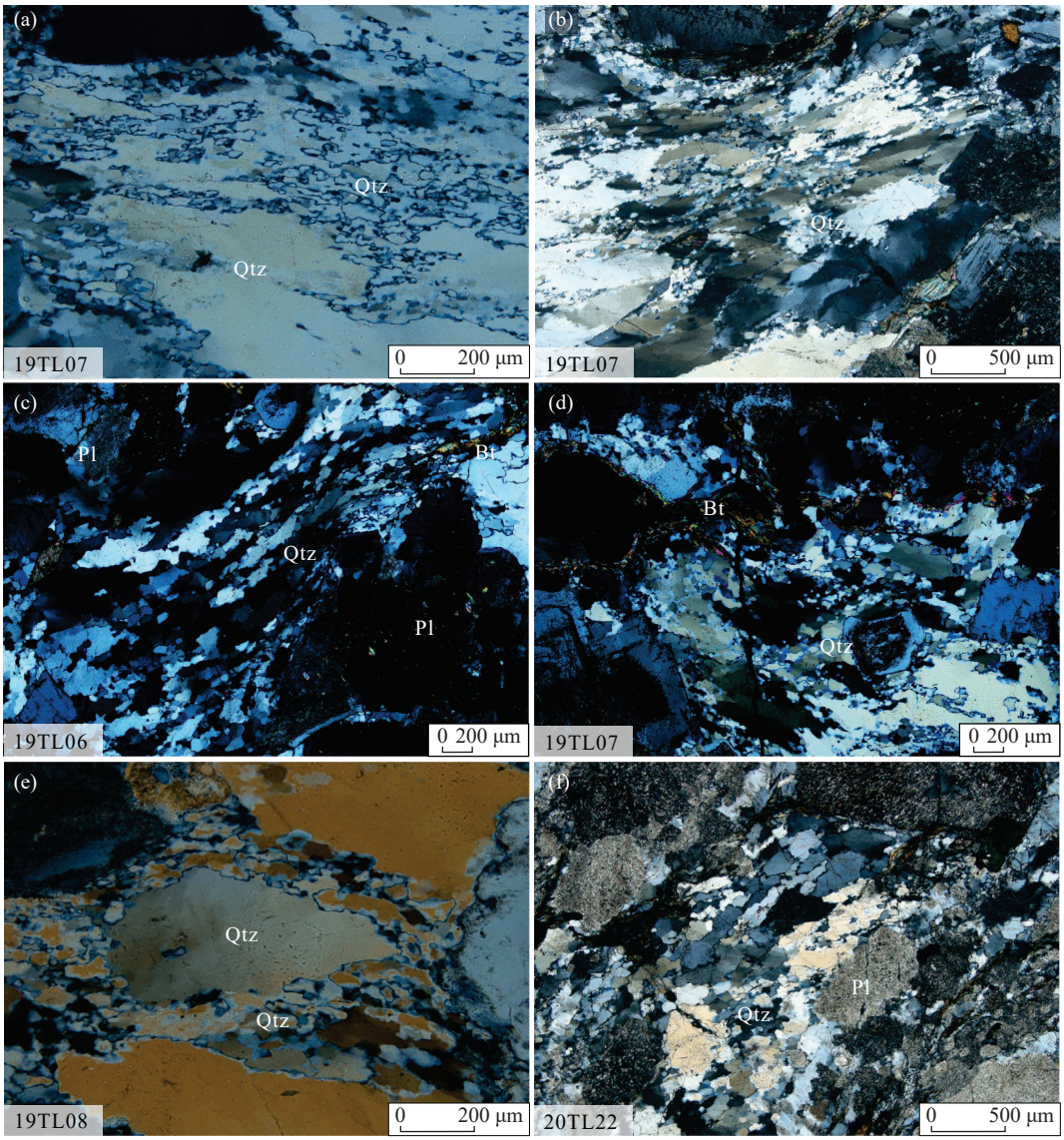

Fig. 5. Photomicrographs showing recrystallization of quartzes in mylonites. (a) Sub-particle rotational recrystallization; (b) expansion type recrystallization; (c) particle boundary migration rejunction crystal; (d) subparticle rotational recrystallization; (e) Nuclear mantle structure composed of subparticle rotational recrystallization; (f) Particle boundary migration recrystallization.

observed in the field outcrop, the flesh-red K-feldspar remnants from field investigations, and microscopic observations. The ductile shear zone on both the east and west sides of the WYSZ shows sinistral shearing and tectonites, consisting of flesh-red granitic mylonite and granitic protomylonite containing minerals, such as quartz, feldspar, hornblende, and biotite. Microscopic observation also reveals sericitization in feldspar.

A multi-method analysis was used to estimate the deformation temperature, including the mineral deformation thermometer and EBSD quartz fabric maps. The deformation characteristics of quartz provided a first-order estimation, with microstructures and EBSD analyses indicating that the shear zone developed at mediate to high temperatures in the middle crust. Seven samples of the ductile shear zone were calculated, resulting in differential stresses of 20–40 MPa. The EBSD results also suggest that the east side of the ductile shear zone has lower stress than the west side, indicating stress inhomogeneity within the shear zone.

6.2. Timing of the WYSZ

The two undeformed dikes within the WYSZ (Figs. 2d–f–j) yielded zircon U-Pb ages of 163.9 ± 2.6 Ma, 165.4 ± 4.0 Ma, and 163.1 ± 0.9 Ma (Fig. 9), indicating the emplacement of the dikes at ca. 165 ± 4 Ma. Regrettably, due to inadequate exposure of the dikes or strain localization within the shear zone, the cross-cutting relationship between the dikes and the shear zone is not well defined. If the dikes were involved in the shearing process, the timing of the shear zone postdates the approximate age of 165 ± 4 Ma. Conversely, if the dikes intruded into the shear zone and remained undeformed, the timing of the deformation predates the age of approximately 165 ± 4 Ma. However, the previous studies of crystallization and emplacement ages of the mylonite samples within the WYSZ are 176–160 Ma (Gu CC et al., 2016; Table 3), but the

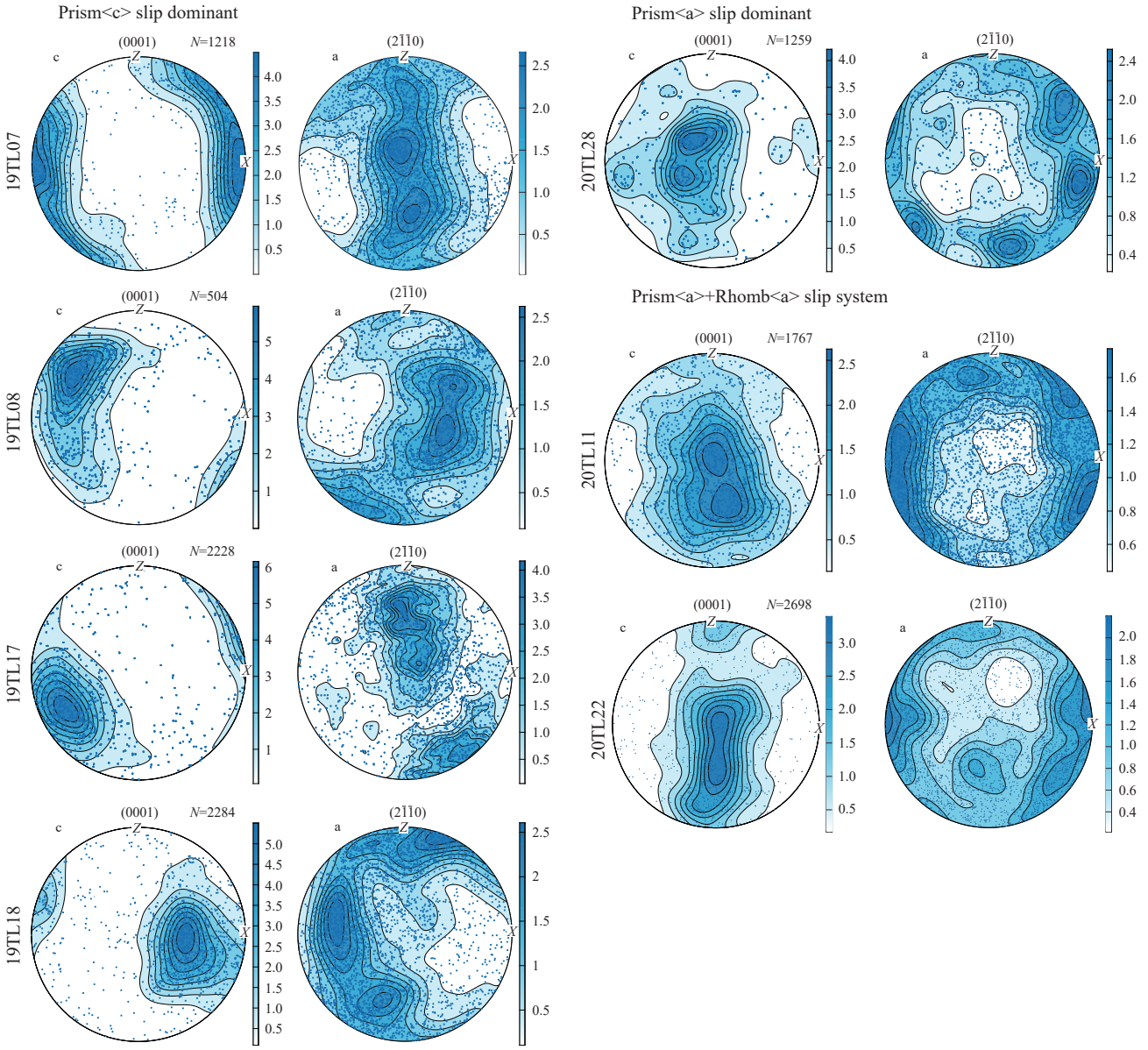

Fig. 6. Polar figures of c-axis fabrics for representative samples of protomylonite, mylonite, and ultramylonite from the WYSZ for comparison. The scale bar shows the pole density.

undeformed granitoids yielded zircon U-Pb ages of ca.125–121 Ma, indicating the WYSZ was active after ca. 176–160 Ma and before ca. 125–121 Ma. Thus, this study proposes that the duration of shearing in the WYSZ requires novel methodologies to offer additional constraints. Muscovite $^{40}Ar/^{39}Ar$ dating on mylonites is proposed as a potential avenue for further investigation.

6.3. Tectonic implications

The WYSZ studied in this research is a result of the sinistral strike-slip movement of the Yilan-Yitong fault zone. The formation time of the WYSZ corresponds to the first phase of sinistral strike-slip of the Yilan-Yitong fault zone, which is loosely constrained between 160~125 Ma and may have occurred in the earliest Cretaceous based on regional geological correlation (Gu CC et al., 2016). As Late Jurassic sediments have not been found, the exposure of the ductile shear zone is the result of uplift and denudation afterward. The brittle faults and positive palm-tree structures were gradually denuded to expose the mylonites in the middle crust. During the Cretaceous, regional extensions occurred, which led to the formation of a series of grabens in this area, including the NE-trending Weiyuanpu-Yehe graben with terrestrial sediments, such as Early Cretaceous Yehe and Quantou Formations. The mylonites exposed in this study area are only in the ascending plate on both sides of the graben, while the main part of the shear zone is buried in the long and narrow graben. A series of thrust nappes were discovered in the region, but no Paleogene sediments were found. The regional geology and available data in this study area indicate that the Yilan-Yitong fault zone was formed by the sinistral shearing during the latest Jurassic to the earliest Cretaceous, exhumed and eroded the brittle faults on the surface, and formed a series of narrow grabens in the Early

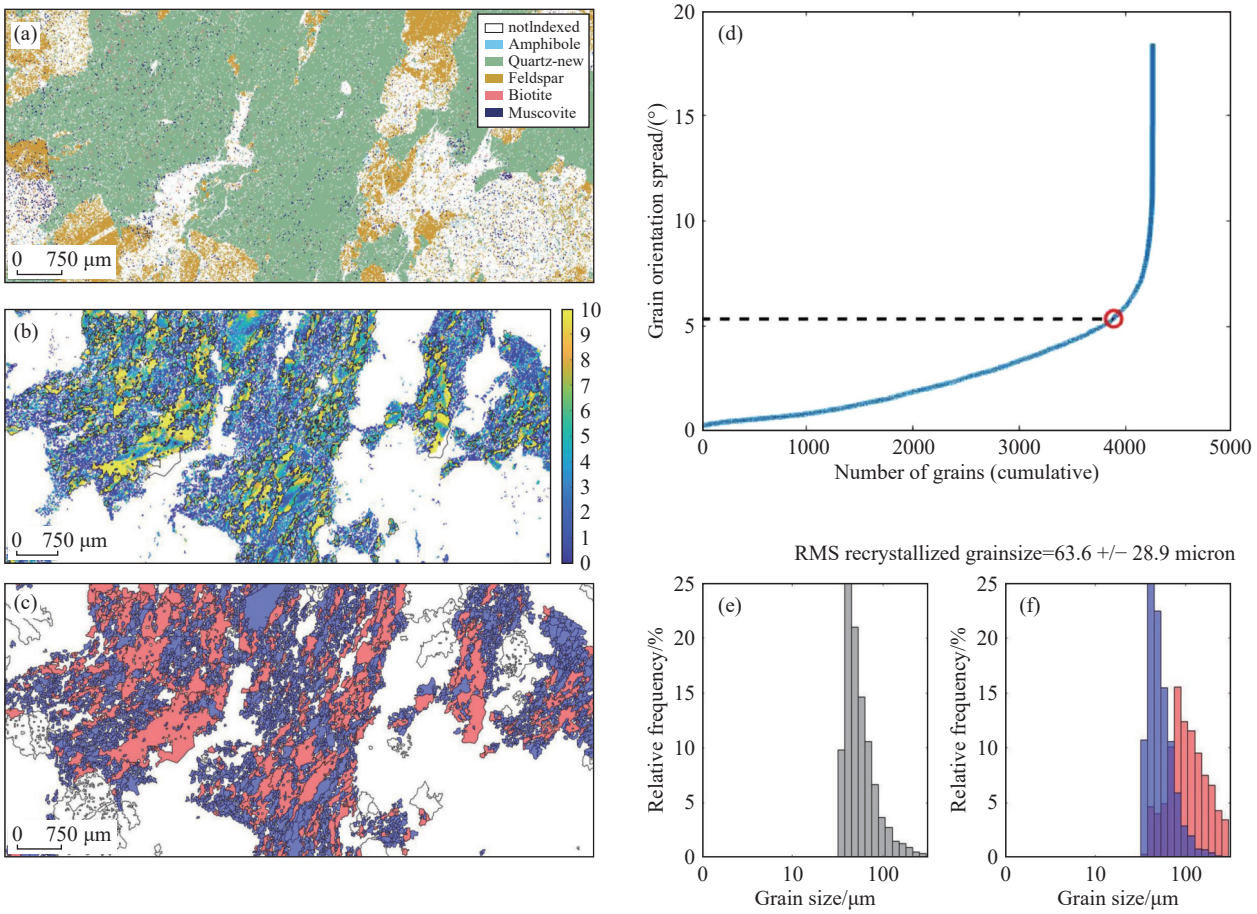

Fig. 7. Recrystallized quartz grain size data and associated microstructures for representative mylonites. (a) Phase diagram of sample 19TL07 minerals from EBSD analysis; (b) Orientation distribution (GOS) of each grain; (c) Distribution of recrystallized particles (blue) and residual particles (red) separated by GOS; (d) Cumulative plot of sample 19TL07 particle count vs. particle orientation distribution; (e) Grain size distribution histogram of all particles for sample 19TL07; (f) Grain size distribution histogram of residual and recrystallized grain of sample 19TL07.

Table 2. EBSD sample and differential stress.

Sample #	Grain size (μm)	Uncertainty (μm)	Number of grains	Differential Stress (MPa)
19TL07	63.6	28.9	3642	31.2
19TL08	53.5	26.5	2783	35.3
19TL17	44.8	16	657	39.9
19TL18	75.4	42.6	1213	27.6
20TL11	116	52.8	1554	20.4
20TL22	111	68	2145	21.1
20TL28	124	65.9	198	19.4

Cretaceous. Subsequently, the fault zone was subjected to compression, forming a series of thrust faults since the Early Cretaceous (Xu M et al., 2017).

Prominent strike-slip fault zones, spanning over 1000 km, such as San Andreas fault in North America (Bergh SG et al., 2019), North Anatolian fault in Turkey (Sengör A, 1979; Hubert-Ferrari A et al., 2002), Altyn Tagh fault in Tibetan Plateau (Yin A et al., 2002; Zhang P et al., 2007), and Tan-Lu fault in East Asia (Xu J et al., 1987; Xu J and Zhu G, 1994), serve as crucial indicators of deformation and displacement in their surrounding blocks. Grasping the evolution of these expansive regional strike-slip fault zones holds pivotal significance in unraveling tectonic transformations (Li C et al., 2023). The Tan-Lu fault and the San Andreas fault are two prominent geological features with similar and distinct characteristics. Both faults are major tectonic boundaries with significant movements between adjacent plates and the potential for substantial seismic activity. Key differences between them is their linkage, seismic characteristics, and tectonic setting; the Tan-Lu fault developed within the Eurasian plate (Wang J and Main I, 2023), whereas the San Andreas fault represents the boundary between the North American and Pacific plates (Khoshmanesh M and Shirzaei M, 2018). Understanding these differences and similarities of their pre-existing structures is crucial for improving earthquake preparedness and mitigating potential risks in the regions they affect (Sun M et al., 2018).

Fig. 8. The CL images of zircon grains from pluton and vein within the WYSZ.

7. Conclusion

This study presents field mapping, macro- and micro-structures, quartz c-axis fabrics, and zircon U-Pb geochronology of the Weiyuanpu-Yehe shear zone in the northern Tan-Lu fault system. The 25 km-long and 1–2 km-wide NE-trending Weiyuanpu-Yehe ductile shear zone cuts through Triassic and Jurassic granite plutons, and is associated with Late Jurassic dikes. The lineation and the mylonitic foliation indicate the sinistral strike-slip motion. Multi-methods suggest that the deformation temperature of mylonite is medium to high. The differential stress of the shear zone is 20–40 MPa. Additionally, the understanding of the geometry of pre-existing structures and deformation history has implication for the predicating of potential earthquakes for the Tan-Lu fault system.

CRediT authorship contribution statement

Liang Qiu, Dan-Ping Yan, Wei Gan, Chengming Li, Rong Chu, and Rui Zhang designed the research and wrote, reviewed, and edited the manuscript. Tianheng Wang, Xiaoyu Chen, and Yu Fu conducted lab work and analyzed data. Yu Fu, Ruoyan Kong, Shouheng Sun, and Xiaoyu Dong did the field investigation.

Declaration of competing interest

The authors declare no conflicts of interest.

Supplementary dataset

Supplementary data to this article can be found online at http://chinageology.cgs.cn/ or available on request from the authors.

Acknowledgments

This study was supported by funding from the NSFC (42030306 and 41672216) and the National Key R&D Program of China (2016YFC0600102-03). We thank Huilong

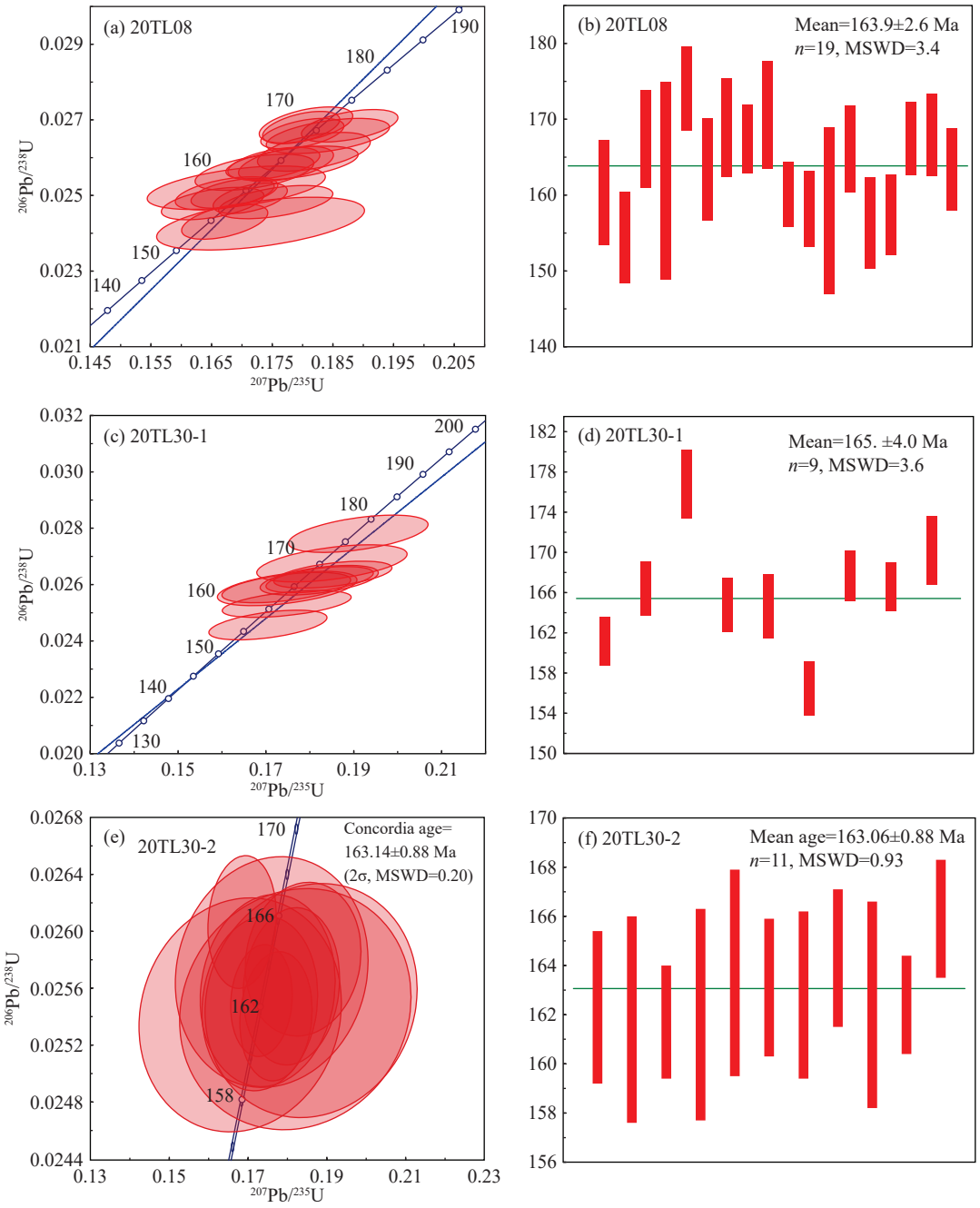

Fig. 9. Zircon U-Pb ages of pluton and vein within the WYSZ in northern Tan-Lu fault system.

Liu, Wenjing Yang, and Yini Wang for fieldwork assistance and Wenrong Cao for providing the Matlab code for the quartz palaeopiezometry. We appreciate constructive comments from Danyal Akram, Hao Feng, Xiao-yu Chen, and anonymous reviewers for the early draft.

References

Bachmann F, Hielscher R, Jupp PE, Pantleon W, Schaeben H, Wegert E. 2010. Inferential statistics of electron backscatter diffraction data from within individual crystalline grains. Journal of Applied Crystallography, 43(6), 1338–1355. doi: 10.1107/S00218898100 3027X.

Bachmann F, Hielscher R, Schaeben H. 2011. Grain detection from 2d and 3d EBSD data —Specification of the MTEX algorithm. Ultramicroscopy, 111, 1720–1733. doi: 10.1016/j.ultramic.2011. 08.002.

Bachmann F, Hielscher R, Schaeben H. 2010. Texture Analysis with MTEX —Free and Open Source Software Toolbox. Solid State Phenomena, 160, 63–68. doi: 10.4028/www.scientific.net/SSP. 160.63.

Bergh, SG, Sylvester, AG, Damte, A, Indrevær, K. 2019. Polyphase kinematic history of transpression along the Mecca Hills segment of the San Andreas fault, southern California. Geosphere 15, 901–934. doi:10.1130/GES02027.1.

BGMRLN. 1973. Regional geological map and report of the Zhuanghe area. scale 1: 20, 000 (in Chinese with English abstract).

BGMRLN. 2014. Regional Geology of the Liaoning Province. Geological Publishing House, 1–1428 (in Chinese with English abstract).

Cai Z, Xu Z, Cao H, Robinson AC, Li G, Xu X. 2017. Miocene

Table 3. Sample information for age constraints from the Yilan-Yitong shear zone in northern Tan-Lu fault system.

Sample No.	Locality	Shear zone location	Rock type	Deformation	Age (Ma)	Data source
YY022	42°41′4.8″N, 124°17′19.7″E	Weiyuanpu-Yehe	Granite	Protomylonite	160.2±1.6	Gu CC et al., 2016
YY127	42°59′19.7″N, 124°35′29.9″E	Weiyuanpu-Yehe	Granite	Mylonite	161.4±1.4	Gu CC et al., 2016
YY136	42°49′53.9″N, 124°23′54.4″E	Weiyuanpu-Yehe	Granite	Mylonite	165.4±2.5	Gu CC et al., 2016
YY131	42°54′15.1″N, 124°27′13.1″E	Weiyuanpu-Yehe	Granite	Mylonitization	168.6±1.7	Gu CC et al., 2016
YY116	42°41′9.9″N, 124°14′38.6″E	Weiyuanpu-Yehe	Granite	Mylonite	173.4±1.8	Gu CC et al., 2016
YY114	42°43′36.7″N, 124°17′30.2″E	Weiyuanpu-Yehe	Granite	Mylonite	175.5±1.9	Gu CC et al., 2016
YY025	42°46′38.3″N, 124°21′46.2″E	Weiyuanpu-Yehe	Granite	Mylonite	257.1±2.7	Gu CC et al., 2016
NT019	42°49′11.0″N, 124°24′7.3″E	Weiyuanpu-Yehe	Granite porphyry	Undeformed	125.6±1.5	Gu CC et al., 2016
YY022	42°41′4.8″N, 124°17′19.7″E	Weiyuanpu-Yehe	Diabase	Undeformed	121.2±3.4	Gu CC et al., 2016
YY132	42°53′3.7″N, 124°26′15.2″E	Weiyuanpu-Yehe	Dioritic dike	Undeformed	122.0±3.3	Gu CC et al., 2016
YY129	42°57′52.7″N, 124°30′48.0″E	Out of Weiyuanpu-Yehe	Granite	Undeformed	192.6±2.0	Gu CC et al., 2016
YY049	44°23′42.0″N, 126°52′27.1″E	Shulan	Granite	Protomylonite	359.1±3.8	Gu CC et al., 2016
YY145	44°31′7.8″N, 127°03′6.0″E	Out of Shulan	Granite	Undeformed	187.4±2.6	Gu CC et al., 2016
20TL08	42°50′3.8″N, 124°23′43.7″E	Weiyuanpu-Yehe	diorite porphyrite dyke	undeformed	163.9±2.6	This study
20TL30-1	42°39′43.3″N, 124°17′42.4″E	Weiyuanpu-Yehe	diorite porphyrite dyke	undeformed	165.4±4.0	This study
20TL30-2	42°39′43.3″N, 124°17′42.4″E	Weiyuanpu-Yehe	diorite porphyrite dyke	undeformed	163.1±0.9	This study

exhumation of northeast Pamir: Deformation and geo/thermochronological evidence from western Muztaghata shear zone and Kuke ductile shear zone. Journal of Structural Geology, 102, 130–146. doi: 10.1016/j.jsg.2017.07.010.

Carreras J, Czeck DM, Druguet E and Hudleston P J. 2010. Structure and development of an anastomosing network of ductile shear zones. Journal of Structural Geology, 32, 656–666. doi: 10.1016/j.jsg.2010.03.013.

Chang EZ, 1996. Collisional orogene between north and south China and its eastern extension in the Korean Peninsula. Journal of Southeast Asian Earth Sciences, 13, 267–277. doi:10.1016/0743-9547(96)00033-5.

Clinkscales C, Kapp P. 2019. Structural style and kinematics of the Taihang-Luliangshan fold belt, North China: Implications for the Yanshanian orogeny. Lithosphere, 11, 767–783. doi: 10.1130/L1096.1.

Cross AJ, Prior DJ, Stipp M, Kidder S. 2017. The recrystallized grain size piezometer for quartz: An EBSD-based calibration. Geophysical Research Letters, 44, 6667–6674. doi: 10.1002/2017gl073836.

Deng YF, Fan W, Zhang Z, Badal J. 2013. Geophysical evidence on segmentation of the Tancheng-Lujiang fault and its implications on the lithosphere evolution in East China. Journal of Asian Earth Sciences, 78, 263–276. doi: 10.1016/j.jseaes.2012.11.006.

Faure M, Lin W, Schärer U, Shu L, Sun Y, Arnaud N, 2003. Continental subduction and exhumation of UHP rocks. Structural and geochronological insights from the Dabieshan (East China). Lithos, 70(3–4), 213–241. doi:10.1016/S0024-4937(03)00100-2.

Gilder SA, Leloup PH, Courtillot V. 1999. Tectonic evolution of the Tancheng-Lujiang (Tan-Lu) fault via middle Triassic to Early Cenozoic paleomagnetic data. Geophys. Res. Solid Earth, 104, 365–390. doi: 10.1029/1999JB900123.

Gu CC, Zhu G, Zhai MJ, Lin SZ, Song LH. 2016. Features and origin time of Mesozoic strike-slip structures in the Yilan-Yitong Fault Zone. Science China. Earth Sciences, 59, 2389–2410. doi: CNKI:SUN:JDXG.0.2016-12-010. doi: 10.1007/s11430-016-5334-4.

Gu CC, Zhu G, Zhang S, Liu C, Li Y, Lin S, Wang W. 2017. Cenozoic evolution of the Yilan–Yitong Graben in NE China: An example of graben formation controlled by pre-existing structures. Journal of Asian Earth Sciences, 146, 168–184. doi: 10.1016/j.jseaes.2017.05.024.

Hacker BR, Ratschbacher L, Webb L, McWilliams MO, Ireland T, Calvert A, Dong S, Wenk HR, Chateigner D. 2000. Exhumation of ultrahigh-pressure continental crust in east central China: Late Triassic-Early Jurassic tectonic unroofing. Journal of Geophysical Research: Solid Earth, 105(B6), 13339–13364. doi: 10.1029/2000jb900039.

Hu W, Li P, Rosenbaum G, Liu J, Jourdan F, Jiang Y, Wu D, Zhang J, Yuan C, Sun M. 2020. Structural evolution of the eastern segment of the Irtysh Shear Zone: Implications for the collision between the East Junggar Terrane and the Chinese Altai Orogen (northwestern China). Journal of Structural Geology, 139, 104126. doi: 10.1016/j.jsg.2020.104126.

Hubert-Ferrari A, Armijo R, King G, Meyer B, Barka A. 2002. Morphology, displacement, and slip rates along the North Anatolian Fault, Turkey. Journal of Geophysical Research:Solid Earth, 107(B10), ETG–9. doi: 10.1002/grl.50882.

Khoshmanesh, M. and Shirzaei, M. 2018. Multiscale dynamics of aseismic slip on Central San Andreas Fault. Geophysical Research Letters, 45(5), 2274–2282. doi: 10.1002/2018GL077017.

Kong RY, Yan DP, Qiu L, Wells ML, Wang AP, Dong XY, Mu HX, Gong LX. 2020. Early Cretaceous tectonic transition and SW-ward basin migration in northern Liaodong Peninsula, NE China: Sedimentary, structural, and geochronological constraints. Geological Journal, 55, 5681–5702. doi: 10.1002/gj.3620.

Li C, Zhang C, Cope TD. 2023. A new model for the segmentation, propagation and linkage of the Tan-Lu fault zone, East Asia. Journal of Asian Earth Sciences, 241, 105466. doi: 10.1016/j.jseaes.2022.105466.

Li S, Suo Y, Li X, Zhou J, Santosh M, Wang P, Wang G, Guo L, Yu S, Lan H, Dai L. 2019. Mesozoic tectono-magmatic response in the East Asian ocean-continent connection zone to subduction of the Paleo-Pacific Plate. Earth-Science Reviews, 192, 91–137. doi: 10.1016/j.earscirev.2019.03.003.

Li S, Zhao G, Dai L, Liu X, Zhou L, Santosh M, Suo Y. 2012. Mesozoic basins in eastern China and their bearing on the deconstruction of the North China Craton. Journal of Asian Earth Sciences, 47, 64–79. doi: 10.1016/j.jseaes.2011.06.008.

Li Y, Zhu G, Su N, Xiao S, Zhang S, Liu C, Xie C, Yin H, Wu X. 2019. The Xiaoqinling metamorphic core complex: A record of Early Cretaceous backarc extension along the southern part of the North China Craton. Geological Society of America Bulletin, 132, 617–637. doi: 10.1130/B35261.1.

Li ZX, 1994. Collision between the north and south blocks: A crust-detachment model for suturing in the region east of the Tan-Lu fault. Geology 22 (8), 739–742. doi: 10.1130/0091-7613(1994)022<0739:cbtnas>2.3.co;2.

Liang S, Gan W, Wang C. 2020. Characterizing subseismic faults from SK-2 drilling core (2900–4200 m): Implication for reservoir transmissibility and regional tectonic evolution. Interpretation, 8, SG1–SG11. doi: 10.1190/int-2019-0098.1.

Lin SF, 1995. Collision between the North and South China blocks: a crustal-detachment model for suturing in the region east of the Tanlu fault: Comment. Geology 23 (6), 574–576. doi: 10.1130/0091-7613(1994)0222.3.CO;2.

Liu C, Zhu G, Zhang S, Gu C, Li Y, Su N, Xiao S. 2018. Mesozoic strike-slip movement of the Dunhua–Mishan Fault Zone in NE China: A response to oceanic plate subduction. Tectonophysics, 723, 201-222. https://doi.org/10.1016/j.tecto.2017.12.024.

Liu J, Chen X, Tang Y, Song Z, Wang W. 2020. The Ailao Shan–Red River shear zone revisited: Timing and tectonic implications. GSA Bulletin, 132(5-6), 1165–1182. doi: 10.1130/B35220.1.

Meng E, Xu WL, Pei FP, Yang DB, Yu Y, Zhang XZ. 2010. Detrital-zircon geochronology of Late Paleozoic sedimentary rocks in eastern Heilongjiang Province, NE China: Implications for the tectonic evolution of the eastern segment of the Central Asian Orogenic Belt. Tectonophysics, 485, 42–51. doi: 10.1016/j.tecto.2009.11.015.

Okay AI and Celal Şengör AM. 1992. Evidence for intracontinental thrust-related exhumation of the ultra-high-pressure rocks in China. Geology, 20(5), 411–414. doi: 10.1130/0091-7613(1992)020<0411:EFITRE>2.3.CO;2.

Paton C, Woodhead JD, Hellstrom JC, Hergt JM, Greig A and Maas R. 2010. Improved laser ablation U-Pb zircon geochronology through robust downhole fractionation correction. Geochemistry Geophysics Geosystems 11, Q0AA06. doi: 10.1130/0091-7613(1992)020<0411:EFITRE>2.3.CO;2.

Qiu L, Kong RY, Yan DP, Wells ML, Wang AP, Sun W, Yang WX, Han YG, Li C, Zhang Y, Ariser S. 2018. The Zhayao tectonic window of the Jurassic Yuantai thrust system in Liaodong Peninsula, NE China: Geometry, kinematics and tectonic implications. Journal of Asian Earth Sciences, 164, 58–71. doi: 10.1016/j.jseaes.2018.06.012.

Qiu L, Yan DP, Tang SL, Chen F, Song ZD, Gao T, Zhang YX. 2020. Insights into post-orogenic extension and opening of the Palaeo-Tethys Ocean recorded by an Early Devonian core complex in South China. Journal of Geodynamics, 135, 101708. doi: 10.1016/j.jog.2020.101708.

Qiu L, Kong R, Yan DP, Mu HX, Sun W, Sun S, Han Y, Li C, Zhang L, Cao F, Ariser S. 2022. Paleo-Pacific plate subduction on the eastern Asian margin: Insights from the Jurassic foreland system of the overriding plate. GSA Bulletin, 134 (9–10), 2305–2320. doi: 10.1130/B36118.1.

Ramsay JG, Graham RH. 1970. Strain variation in shear belts. Canadian Journal of Earth Sciences, 7, 786–813. doi: 10.1139/e70-078.

Ramsay J. 1980. Shear zone geometry: a review. Journal of Structural Geology, 2(1–2), 83–99. doi:10.1016/0191-8141(80)90038-3.

Ren J, Tamaki K, Li S, Zhang J. 2002. Late Mesozoic and Cenozoic rifting and its dynamic setting in Eastern China and adjacent areas. Tectonophysics, 344, 175–205. doi: 10.1016/S0040-1951(01)00271-2.

Sengör AMC, 1979. The North Anatolian transform fault: its age, offset and tectonic significance. Journal of the Geological Society, 136(3), 269–282. doi:10.1144/gsjgs.136.3.0269.

Sibson RH. 1977. Fault rocks and fault mechanisms. Journal of the Geological Society, 133, 191–213. doi: 10.1144/gsjgs.133.3.0191.

Simonetti M, Carosi R, Montomoli C, Corsini M, Petroccia A, Cottle JM, Iaccarino S. 2020. Timing and kinematics of flow in a transpressive dextral shear zone, Maures Massif (Southern France). International Journal of Earth Sciences, 109, 2261–2285. doi: 10.1007/s00531-020-01898-6.

Simonetti M, Carosi R, Montomoli C, Law RD, Cottle JM. 2021. Unravelling the development of regional-scale shear zones by a multidisciplinary approach: the case study of the Ferriere-Mollières Shear Zone (Argentera Massif, Western Alps). Journal of Structural Geology, 104399. doi: 10.1016/j.jsg.2021.104399.

Sláma J, Kosler J, Condon D J, Crowley J L, Gerdes A, Hanchar J M, Horstwood M S A, Morris G A, Nasdala L, Norberg N, Schaltegger U, Schoene B, Tubrett M N, Whitehouse M J., 2008. Plesovice zircon--A new natural reference material for U-Pb and Hf isotopic microanalysis. Chemical Geology 249, 1–35. doi: 10.1016/j.chemgeo.2007.11.005.

Stipp M, Stünitz H, Heilbronner R, Schmid SM, 2002. Dynamic recrystallization of quartz: correlation between natural and experimental conditions. Geological Society, London, Special Publications, 200(1), 171–190. doi: 10.1144/GSL.SP.2001.200.01.11.

Sun M, Yin A, Yan D, Ren H, Mu H, Zhu L, Qiu L. 2018. Role of pre-existing structures in controlling the Cenozoic tectonic evolution of the eastern Tibetan plateau: new insights from analogue experiments. Earth and Planetary Science Letters, 491, 207–215. doi: 10.1016/j.epsl.2018.03.005.

Suo Y, Li S, Cao XZ and Wang X, Somerville I, Wang G, Liu P, Liu B. 2020. Mesozoic-Cenozoic basin inversion and geodynamics in East China: A review. Earth-Science Reviews, 210, 103357. doi: 10.1007/s11430-014-4903-7.

Thompson J, Meffre S, Danyushevsky L., 2018. Impact of air, laser pulse width and fluence on U-Pb dating of zircons by LA-ICPMS. Journal of Analytical Atomic Spectrometry, 33, 221–230. doi: 10.1039/c7ja00357a.

Wang J and Main IG. 2023. Strong historical earthquakes and their relationships with the Tan-Lu fault system and modern seismicity in eastern China. Natural Hazards, 115(1), 564. doi: 10.1007/s11069-022-05565-8.

White SH, Burrows SE, Carreras J, Shaw ND, Humphreys FJ. 1980. On mylonites in ductile shear zones. Journal of structural geology, 2(1–2), 175–187. doi:10.1016/0191-8141(80)90048-6.

Wu FY, Sun DY, Ge WC, Zhang YB, Grant ML, Wilde SA, Jahn BM. 2011. Geochronology of the Phanerozoic granitoids in northeastern China. Journal of Asian Earth Sciences, 41, 1–30. doi: 10.1016/j.jseaes.2010.11.014.

Xiao WJ, Windley B., Hao J, Zhai MG. 2003. Accretion leading to collision and the Permian Solonker suture, Inner Mongolia, China: Termination of the Central Asian orogenic belt. Tectonics, 22(6), 8(1–20). doi: 10.1029/2002TC001484, 2003.

Xu JW, Zhu G, Tong WX, Cui K, Liu Q. 1987. Formation and evolution of the Tancheng-Lujiang wrench fault system: a major shear system to the northwest of the Pacific Ocean. Tectonophysics, 134, 273–310. doi: 10.1016/0040-1951(87)90342-8.

Xu JW, Zhu G. 1994. Tectonic Models of the Tan-Lu Fault Zone, Eastern China. International Geology Review, 36, 771–784. doi: 10.1080/00206819409465487.

Xu M, Li Y, Hou H, Wang C, Gao R, Wang H, Han Z, Zhou A. 2017. Structural characteristics of the Yilan–Yitong and Dunhua–Mishan faults as northern extensions of the Tancheng–Lujiang Fault Zone: New deep seismic reflection results. Tectonophysics, 706, 35–45. doi: 10.1016/j.tecto.2017.03.018.

Yan DP, Qiu L. 2020. Geology of China and adjacent regions: An introduction. Journal of Asian Earth Sciences, 203, 1–3. doi: 10.2343/geochemj.38.417.

Yan DP, Kong RY, Dong XY, Qiu L, Liu HL. 2021. Late Jurassic-Early Cretaceous tectonic switching in Liaodong Peninsula of the North China Craton and the implications for gold mineralisation. Science China Earth Sciences, 9, 1–20. doi:10.1007/s11430-020-9770-6.

Yin A. , Nie S. 1993. An indentation model for the North and South China collision and the development of the Tan-Lu and Honam fault systems, eastern Asia. Tectonics, 12, 801–813. doi: 10.1029/93TC00313.

Yin A, Rumelhart PE, Butler R, Cowgill E, Harrison TM, Foster DA,

Ingersoll RV, Zhang Q, Zhou XQ, Wang XF, Hanson A. 2002. Tectonic history of the Altyn Tagh fault system in northern Tibet inferred from Cenozoic sedimentation. Geological Society of America Bulletin, 114(10), 1257–1295. doi: 10.1130/0016-7606(2002)114<1257:THOTAT>2.0.CO;2.

Zhang B, Zhu G, Jiang D, Li C, Chen Y. 2012. Evolution of the Yiwulushan metamorphic core complex from distributed to localized deformation and its tectonic implications. Tectonics, 31, 1–22. doi: 10.1029/2012tc003104.

Zhang S, Zhu G, Xiao S, Su N, Liu C, Wu X, Yin H, Li Y, Lu Y. 2020. Temporal variations in the dynamic evolution of an overriding plate: Evidence from the Wulong area in the eastern North China Craton, China. GSA Bulletin, 132, 2023–2042. doi: 10.1130/B35465.1.

Zhang PZ, Molnar P, Xu X. 2007. Late Quaternary and present-day rates of slip along the Altyn Tagh Fault, northern margin of the Tibetan Plateau. Tectonics, 26(5), 1–24. doi: 10.1029/2006TC002014.

Zhao T, Zhu G, Lin S, Wang H. 2016. Indentation-induced tearing of a subducting continent: Evidence from the Tan-Lu Fault Zone, East China. Earth-Science Reviews, 152, 14–36. doi: 10.1016/j.earscirev.2015.11.003.

Zhu, G. , Hu, W. , Song, L. , Liu, B. , 2015. Quaternary activity along the Tan-Lu fault zone in the Bohai Bay, East China: Evidence from seismic profiles. Journal of Asian Earth Sciences 114, 5–17. doi: 10.1016/j.jseaes.2015.03.030.

Zhu G, Liu C, Gu C, Zhang S, Li Y, Su N, Xiao S. 2018. Oceanic plate subduction history in the western Pacific Ocean: Constraint from late Mesozoic evolution of the Tan-Lu Fault Zone. Science China Earth Sciences, 61, 386–405. doi: 10.1007/s11430-017-9136-4.

Zhu G, Wang Y, Liu G, Niu M, Xiu C, Li C. 2005. $^{40}Ar/^{39}Ar$ dating of strike-slip motion on the Tan-Lu fault zone, East China. Journal of Structural Geology, 27, 1379–1398. doi: 10.1016/j.jsg.2005.04.007.